9716–9732 *Nucleic Acids Research, 2023, Vol. 51, No. 18* *Published online 18 August 2023*
https://doi.org/10.1093/nar/gkad679

Structure-specific roles for PolG2–DNA complexes in maintenance and replication of mitochondrial DNA

Jessica L. Wojtaszek[1,†], Kirsten E. Hoff[1,†], Matthew J. Longley[1], Parminder Kaur[2,3], Sara N. Andres[1], Hong Wang[2,3,4], R. Scott Williams[1,*] and William C. Copeland[1,*]

[1]Genome Integrity and Structural Biology Laboratory, National Institute of Environmental Health Sciences, National Institutes of Health, Research Triangle Park, NC 27709, USA, [2]Physics Department, North Carolina State University, Raleigh, NC 27695, USA, [3]Center for Human Health and the Environment, North Carolina State University, Raleigh, NC 27695, USA and [4]Toxicology Program, North Carolina State University, Raleigh, NC 27695, USA

Received May 24, 2023; Revised July 13, 2023; Editorial Decision July 31, 2023; Accepted August 09, 2023

ABSTRACT

The homodimeric PolG2 accessory subunit of the mitochondrial DNA polymerase gamma (Pol γ) enhances DNA binding and processive DNA synthesis by the PolG catalytic subunit. PolG2 also directly binds DNA, although the underlying molecular basis and functional significance are unknown. Here, data from Atomic Force Microscopy (AFM) and X-ray structures of PolG2–DNA complexes define dimeric and hexameric PolG2 DNA binding modes. Targeted disruption of PolG2 DNA-binding interfaces impairs processive DNA synthesis without diminishing Pol γ subunit affinities. In addition, a structure-specific DNA-binding role for PolG2 oligomers is supported by X-ray structures and AFM showing that oligomeric PolG2 localizes to DNA crossings and targets forked DNA structures resembling the mitochondrial D-loop. Overall, data indicate that PolG2 DNA binding has both PolG-dependent and -independent functions in mitochondrial DNA replication and maintenance, which provide new insight into molecular defects associated with PolG2 disruption in mitochondrial disease.

GRAPHICAL ABSTRACT

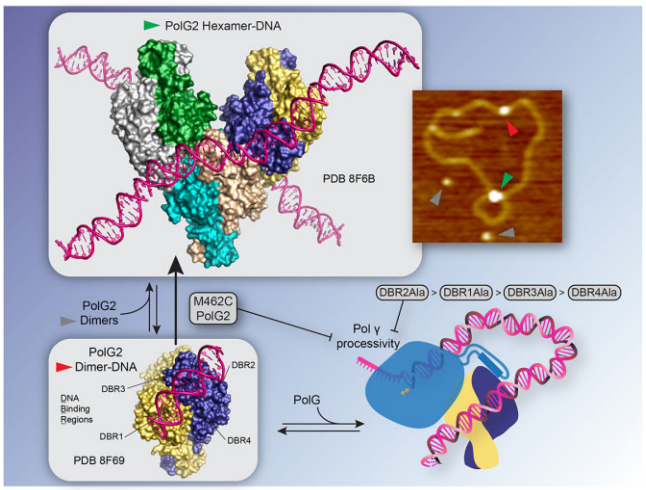

INTRODUCTION

While diploid cells contain pairs of nuclear chromosomes, different cell types can contain hundreds to thousands of copies of mitochondrial DNA (mtDNA). Human mtDNA is a double-stranded, circular 16.5 kb genome that encodes 13 essential components of mitochondrial respiratory chain complexes as well as 22 transfer RNAs and 2 ribosomal RNAs required for translation within mitochondria (1). Mitochondrial genes are transcribed from divergent promotors within a ∼1 kb non-coding region (NCR). Synthesis of nascent mtDNA begins at a sequence-specific origin near the 5′-end of the NCR (2) and ends at a termination-associated sequence (TAS) at the 3′ end of the NCR (3). The resulting single-stranded, linear '7S DNA' replication intermediate can remain hybridized within the NCR to

*To whom correspondence should be addressed. Tel: +1 984 287 4269; Email: copelan1@niehs.nih.gov
Correspondence may also be addressed to R. Scott Williams. Email: williamsrs@niehs.nih.gov
†The authors wish it to be known that, in their opinion, the first two authors should be regarded as Joint First Authors.
Present address: Sara N. Andres, Department of Biochemistry and Biomedical Sciences, McMaster University, Hamilton, Ontario, Canada.

generate a triple-stranded D-loop in some mtDNA molecules (4). Turnover of 7S DNA is regulated by mtDNA replication proteins and other protein factors, and the resulting effects on conformation and stability of the D-loop can influence synthesis and maintenance of full-length mtDNA molecules (5).

Partial reconstitution of the mitochondrial replisome *in vitro* shows coordinated function of DNA Polymerase γ (Pol γ), the Twinkle DNA helicase, and the mitochondrial single-stranded DNA binding protein (6,7). Human Pol γ holoenzyme functions as a heterotrimer comprising a single 140 kDa catalytic subunit PolG (encoded by *POLG*) and a dimeric 55 kDa accessory subunit PolG2 (encoded by *POLG2*). PolG2 functions as a processivity factor by stimulating salt tolerant DNA synthesis and by increasing the affinity of Pol γ to DNA (8,9). Germline mutation of the nuclear genes encoding these proteins disrupts mtDNA synthesis and predisposes cells to mutation, deletion and depletion of mtDNA. Accumulating genetic damage leads to mitochondrial dysfunction and a variety of heritable, age-dependent mitochondrial disorders (10,11). Human *POLG2* was identified as a mitochondrial disease locus in 2006 (12), and now at least 11 clinically relevant missense mutations in *POLG2* have been identified (13–16). In a mouse model, heterozygous *Polg2*$^{+/-}$ knockout mice are haplosufficient and develop normally, whereas homozygous *Polg2*$^{-/-}$ mice are embryonic lethal at day 8.5 p.c. with concomitant loss of mtDNA (17). However, the structural basis for PolG2 dysfunction in disease remains incompletely defined.

The crystal structure of the human Pol γ holoenzyme reveals asymmetric interaction of the PolG catalytic subunit with PolG2 dimers, wherein PolG has extensive contact with the proximal PolG2 monomer and limited contact with the distal PolG2 monomer (18). Biochemical analysis shows that the proximal PolG2 monomer increases the affinity of the holoenzyme for DNA, and the distal PolG2 monomer serves to increase the polymerization rate of the holoenzyme (19). The structure of the PolG-PolG2–DNA ternary complex verifies that the proximal PolG2 monomer scaffolds PolG interactions with DNA (20). However, no direct DNA binding is mediated by PolG2 in these structures, which appears to conflict with a large body of evidence indicating that PolG2 binds double-stranded DNA (dsDNA) (8), folded secondary structure within single-stranded DNA (ssDNA) (21,22), and synthetic D-loop structures *in vitro* (23). Crystal structures of mouse and human PolG2 in the absence of DNA revealed dimeric subunit structures with a large dimeric interface (21,24). Models of electrostatic surface potential suggested putative DNA binding regions for PolG2, and both deletion analysis and targeted alanine substitution confirmed involvement of two loops in DNA binding *in vitro* (21,22). Yet, how PolG2 engages DNA, and the ways this action affects Pol γ functions remain unclear due to the lack of molecular structural information for PolG2–DNA complexes.

To clarify PolG2 functions we determined crystal structures of dimeric and hexameric PolG2–DNA complexes. Our structures unveil an extensive DNA-protein interface and uncover four conserved PolG2 DNA binding regions. Targeted alanine substitution decreases intrinsic DNA-binding affinity and proportionately reduces the ability to stimulate processive DNA synthesis by PolG without diminishing Pol γ subunit affinities *in vitro*. The hexameric structure also predicts a spatial clash that prohibits PolG2 oligomers from binding PolG. Single-molecule analysis by AFM imaging also supports the preferential binding of dimeric PolG2 to linear DNA duplexes and higher order PolG2 oligomers to DNA crossings or forked DNA structures resembling the mitochondrial D-loop. Taken together, our AFM, X-ray crystal structures, and biochemical data indicate that PolG2 DNA-binding has both PolG-dependent and -independent functions and suggest structure-specific DNA-binding roles for PolG2 oligomers.

MATERIALS AND METHODS

Cloning

A cDNA encoding human PolG2 without a mitochondrial targeting sequence but with a C-terminal hexa-histidine affinity tag was maintained in the pET55 expression plasmid (12). A human PolG2 construct without a mitochondrial targeting sequence but with an N-terminal hexa-histidine affinity tag and a TEV protease cleavage sequence was maintained in the pETDuet-1 plasmid. All mutant forms were generated in pETDuet-1 using the NEB Q5 mutagenesis kit (New England Biolabs Cat #E0554S) except DBR2 Ala which was generated with the QuikChange II site-directed mutagenesis kit (Agilent Cat #200523). The primers used to generate the DBR1-4 Ala and M462C PolG2 mutations were: DBR1 Ala forward 5′-agcagcaAATGTGGTTCCTTGTGTTC-3′ and reverse 5′-ccatctgcGCCATGTAATTTAGACAC-3′, DBR2 Ala forward 5′-GAGAACTCCTTTACAG CAGCGGCAAATCTTCATAGAAAGG-3′ and reverse 5′-CCTTTCTATGAAGATTTGCCGCTGCT GTAAAGGAGTTCTC-3′, DBR3 Ala forward 5′-ttggaactagcaCAGGTTTGTCAAGGGCTA-3′ and reverse 5′-tgcggggcctgcTCCTACATCCAAAGCAAC-3′, DBR4 Ala forward 5′-gtccgcaTTGGAACAACT TTATTCGAAG-3′ and reverse 5′-gccatagcTTCC AAATAACCAGGCCAC-3′, and M462C forward 5′-AGACACCACAtgtAAGGAAATGATGCATATATC-3′ and reverse 5′-CTGCTTCTCAGATGTATTAATC-3′. DNA encoding mouse PolG2 with a C-terminal histidine affinity tag was obtained from Daniel Bogenhagen and maintained in the pET22b(+) plasmid. DNA encoding mouse PolG2 with an N-terminal histidine affinity tag and TEV protease cleavage site was maintained in the pMCSG7 plasmid.

Protein expression and purification

Escherichia coli BL21(DE3) transformed with plasmids encoding WT human PolG2, WT mouse PolG2 or mutant forms of human PolG2 lacking mitochondrial targeting sequences were grown in LB media containing 100 μg/ml ampicillin until reaching an OD_{600} between 0.8 and 1.0. Protein expression was induced by addition of isopropyl β-D-1-thiogalactopyranoside to 1 mM and grown overnight at 18°C. Cells were harvested by centrifugation at 3500 × g for 15 min at ambient temperature and stored at −80°C.

Cell pellets from 4.5 l cultures were resuspended in 80 ml lysis buffer (50 mM Tris pH 7.5, 500 mM NaCl, 25 mM imidazole, 1% Triton X-100, 1× Protease Inhibitor Cocktail (Sigma Cat #P8849), 25 μM PMSF) and lysed by sonication (90% amplitude for 1 s, wait 1 s for 20 cycles) on ice. Lysates were clarified by centrifugation at 10 000 × g for 60 min at 4°C. Clarified lysates were incubated with pre-equilibrated nickel resin (3 ml) for 2 h at 4°C. Nickel resin was then collected at 1000 × g for 5 min at 4°C, washed twice with 50 ml of nickel wash buffer 1 (50 mM Tris pH 7.5, 500 mM NaCl, 25 mM imidazole, 1.0% Triton X-100) and once with 50 ml nickel wash buffer 2 (50 mM Tris pH 7.5, 500 mM NaCl, 25 mM imidazole). Washed nickel resin was then resuspended in nickel wash buffer 2 and transferred to an Econo-Column (Bio-Rad Cat #7371512). Protein was eluted by gravity flow using nickel elution buffer (50 mM Tris pH 9.0, 250 mM imidazole) until no further protein was indicated by qualitative Bradford assay. Protein was then digested with TEV protease (20 μg) overnight at 4°C. Protein was further purified using a HiLoad 16/600 Superdex 200 prep grade column (GE Healthcare Cat #28-9893-35) equilibrated in S200 buffer (25 mM KPO_4 pH 7.0, 10% glycerol, 1 mM EDTA, 1 mM 2-mercaptoethanol, 100 mM NaCl). The final purification step was cation exchange on a MonoS 5/50 GL column (GE Healthcare Cat #17–5168-01), utilizing S200 buffer as buffer A and MonoS elution buffer (25 mM KPO_4 pH 7.0, 10% glycerol, 1 mM EDTA, 1 mM 2-mercaptoethanol, 1 M NaCl) as buffer B. The MonoS column was preequilibrated with 0% buffer B, and protein was eluted using a 15 column volume gradient from 0% to 100% buffer B. Buffers with or without 2-mercaptoethanol were used to prepare PolG2 M462C with reduced or oxidized sulfhydryl groups. PolG2 concentrations are expressed as monomers unless otherwise indicated.

Recombinant baculoviruses expressing human PolG containing an N-terminal hexa-histidine affinity tag but lacking a mitochondrial targeting sequence were generated with BacPAK6 (Clontech) viral DNA (25). Hexa-histidine-tagged PolG was purified from baculovirus-infected *Spodoptera frugiperda* Sf9 cells and stored as described previously (26). To simplify biochemical analyses, exonuclease-deficient (D198A/E200A-substituted) human PolG was utilized for all DNA polymerase assays *in vitro* (27).

DNA substrate for AFM imaging

The model DNA replication fork structure on the circular DNA substrate was generated using pBluescript KS-derived plasmid that contains a 398-bp G-less cassette (pGLGAP, a gift from the Griffith group at UNC-Chapel Hill) (28). First, to generate a ssDNA tail, the pGLGAP plasmid was nicked using Nb.BbvCI (NEB), followed by strand-displacement synthesis using the Klenow fragment (exo-, NEB) in a buffer containing dATP, dTTP, and dGTP, but lacking dCTP. A dsDNA tail was created by annealing a primer (5′-CTTCCTCCATCTATACCACC-3′) to the ssDNA tail, followed by extension using the Klenow fragment (exo-) in a buffer containing dATP, dTTP, and dCTP, but lacking dGTP. DNA samples were purified using the Zymo DNA Clean & Concentrator™ kit after each enzymatic reaction step. The resulting DNA substrate is a 3429 bp duplex circle with a 373 bp dsDNA tail, including a 25 nt ssDNA gap at the junction of the circle and the tail (28).

Atomic force microscopy

To assess the oligomeric state of human PolG2, samples of PolG2 with a C-terminal histidine affinity tag were diluted in buffer A containing 50 mM Tris–HCl (pH 7.5), 10% glycerol, 1mM EDTA, 1mM 2-mercaptoethanol, 0.005% Nonidet *P*-40 and 0.1M KCl. To assess binding of PolG2 to DNA substrates, 22 nM PolG2 dimers were premixed with 4.5 nM model DNA substrate in buffer A. Samples were immediately deposited onto freshly cleaved mica surfaces at room temperature, followed by washing with deionized water and drying with streams of nitrogen gas prior to AFM imaging. AFM imaging in the air was carried out using the AC mode on a MFP-3D-Bio AFM (Asylum Research, Oxford Instruments) with Pointprobe® PPP-FMR probes (Nanosensors, spring constants at ∼2.8 N/m). All images were captured at a scan size of 1–3 μm × 1–3 μm, a scan rate of 1–2 Hz, and a resolution of 512 × 512 or 1024 × 1024 pixels, as described previously (29,30). For volume measurements of PolG2 alone and PolG2 with DNA, Gwyddion software was first used to subtract the background. This was achieved by masking the POLG2 (± DNA) complexes in AFM images. Background polynomials were retracted from these masked images. Horizontal noises in AFM images were removed, followed by the plane background subtraction. To measure the volume of PolG2 (± DNA), a mask was applied to the zoomed-in individual PolG2 (± DNA). The extracted volume was exported as a text file and plotted in OriginLab software to generate the AFM volume distribution. Different DNA structures may contribute uncertainty to AFM volume determinations. Volume data are reported as Gaussian peaks ± S.D.

Crystallization

WT murine PolG2 was concentrated to 100 μM and mixed with dsDNA at a 1:1.2 ratio (80 μM PolG2 dimers:96 μM dsDNA) for initial screening. Varying lengths of desalted, blunt-ended dsDNA were tested, including 5, 6, 7, 8, 9, 10, 12, 14, 16, 18, 20, 22, 24, 26, 28 and 30 bp (Integrated DNA Technologies). Initial screening was performed using the NeXtal JCSG core suite I (Qiagen) and the sitting drop vapor diffusion method. Drops contained 1 μl of protein:dsDNA added to 1 μl of well solution. Initial hits of WT murine PolG2 were identified in JCSG core suite I E11 (0.1M MES, pH 5.0 and 20% MPD) with 18 bp dsDNA. Optimized protein-dsDNA crystals were grown in solutions containing 0.1 M MES, pH 5.0–6.5 and 5–30% MPD using the hanging drop vapor diffusion method with PolG2 protein:dsDNA ratios of 1 dimer:2 dsDNA, 1 dimer:1.2 dsDNA and 2 dimers:1 dsDNA.

X-ray crystallography data collection, structure solution and refinement

X-ray data was collected at 105K on beamline 22-ID of the Advanced Photon Source at a wavelength of 1.000 Å. Data

reduction and scaling was performed with the HKL2000 suite (31). The murine PolG2 dimer in complex with 18 bp dsDNA structure was solved by molecular replacement with PDB 1G5I (21) as a model, performed by the PHENIX software suite (32). A combination of density modification with Autobuild and manual refinement in COOT (33) produced a model that was refined to 2.202 Å in PHENIX. The final model (R_{work} = 19.39, R_{free} = 22.83) displays good geometry statistics (RMS_{bonds} = 0.004, RMS_{angles} = 0.64; Ramachandran statistics, 97.39% favored, 0.0% outliers). The murine PolG2 hexamer in complex with 18 bp dsDNA structure was solved by molecular replacement with PDB 1G5I (21) as a model, performed by the PHENIX software suite (32). A combination of density modification with Autobuild and manual refinement in COOT (33) produced a model that was refined to 2.747 Å in PHENIX. The final model (R_{work} = 19.60, R_{free} = 22.16) displays good geometry statistics (RMS_{bonds} = 0.002, RMS_{angles} = 0.43; Ramachandran statistics, 98.22% favored, 0.0% outliers). While the DNA-protein interface is well-defined in the electron density, we observed elevated B-factors and associated RSRZ scores for the flexible helical bundle dimerization insertion domain (Domain 2). Data collection and refinement statistics are provided in detail in Supplemental Table S1. PyMOL was used for final structure model analysis and figure preparation (Schrödinger, LLC). Structures and associated experimental data were deposited in the RCSB PDB with codes 8F69 and 8F6B for the dimer and hexamer, respectively.

Size exclusion chromatography with multiangle light scattering (SEC-MALS)

An Agilent 1100 HPLC was used to inject 100 μl of 1 mg/ml human PolG2 WT and M462C individually onto a WTC-030S5 size exclusion column (Wyatt Technology) with a 1 ml/min flow rate in 25 mM potassium phosphate, pH 7, 200 mM NaCl, 1 mM EDTA running buffer with and without 1 mM TCEP. Samples were buffer exchanged into the respective running buffers prior to injection. The eluate from the column was coupled to a μDAWN MALS detector (Wyatt Technology) and an Optilab RI detector (Wyatt Technology). ASTRA 7 software (Wyatt Technology) was used to collect and analyze light scattering and differential refractive index data according to the manufacturer's instructions. Molecular masses and estimated errors were calculated across individual eluted peaks.

DNA-stimulated oligomerization of PolG2

The presence of disulfide crosslinks at the hexamer interface between PolG2 subunits was assessed by denaturing gels containing SDS but lacking reducing agents. The representative experiments in Figure 3F and Supplementary Figure S6 were conducted by first buffer exchanging human PolG2 WT and M462C into BME-free 25 mM potassium phosphate, pH 7, 200 mM NaCl buffer. 2 μl of 2.6 mg/ml human PolG2 was mixed with 7 μl of buffer and 1 μl of 0–400 μM 47dsDNA (unlabeled) and incubated for 2 h at room temperature. 47dsDNA is a blunt-ended, double-stranded 47 bp DNA substrate originally described by Carrodeguas (22), made by annealing two synthetic oligonucleotides that were purchased from Integrated DNA Technologies: 47F 5′-tat atc caa att aaa agc att ttt gat tgc ata tat atc atc agc ta – 3′ and 47R 5′-tag ctg atg ata tat atg caa tca aaa atg ctt tta att tgg ata ta-3′. To 5 μl of reaction, 1 μl of 300 mM iodoacetamide was added and incubated 30 min at room temperature. Then 2 μl of 4× NuPAGE LDS sample buffer (without reducing reagent) was added and incubated 5 min at room temperature, after which 6 μl was loaded and run on a 15-well denaturing, non-reducing SDS-PAGE gel. The DNA titration experiment was quantified by Image Lab and graphed in Prism.

Electrophoretic mobility shift assay

The DNA binding affinity of PolG2 variants was determined by electrophoretic mobility shift assay (EMSA), essentially as described previously (13). Labeled 47ds-DNA substrate was utilized where oligonucleotide 47F (10 pmol) was 5′-phosphorylated by T4 polynucleotide kinase (NEB Cat #: M0201S) with [γ-^{32}P]ATP (11.1 pmol, 6000 Ci/mmol). Phosphorylated 47F was mixed with 40 pmol unlabeled 47F and 55 pmol unlabeled 47R in 10 mM Tris–HCl pH 7.5, heated at 95°C for 5 min and then allowed to cool to room temperature. DNA binding reactions (10 μl) were assembled on ice and contained 10 mM HEPES pH 8.0, 0.2 mg/ml BSA, 2 mM dithiothreitol (DTT), 174 mM NaCl, 0.15 pmol 47F-47R and varying concentrations of purified PolG2 (0–15 000 nM, as appropriate for each PolG2 variant). Binding reactions with non-reduced M462C PolG2 did not contain DTT. Reactions were placed at room temperature for 10 min prior to addition of 2 μl 5× loading dye (10 mM Tris–HCl pH 7.5, 0.1% bromophenol blue, 50% glycerol). Bound and unbound forms were resolved by native PAGE as previously described (13), imaged on a Typhoon 9400 Phosphorimager (Cytiva), and quantified with NIH Image J software. The fraction of DNA bound was plotted against the concentration of PolG2, and binding isotherms were fit to a quadratic equation by nonlinear regression analysis using the KaleidaGraph program to calculate apparent equilibrium binding constants (34). Reported $K_{d(DNA)}$ values (average ± SEM) are derived from at least triplicate determinations.

Primer extension assay

The ability of PolG2 variants to stimulate DNA synthesis activity of the PolG catalytic subunit was assessed by primer extension reactions *in vitro*, essentially as described previously (13,35). The primer-template substrate was a 5′-end labeled oligonucleotide primer (5′-CCAGTGCCAA GCTTGCATGCCTGCAGGTCGACTCT-3′) hybridized to M13mp18 DNA. The 35mer oligonucleotide (5 pmol) was 5′-phosphorylated by T4 polynucleotide kinase (NEB Cat # M0201S) with [γ-^{32}P]ATP (2.7 pmol, 6000 Ci/mmol). The labeled primer was mixed with M13mp18 single-stranded viral DNA (5.25 pmol) in 10 mM Tris–HCl pH 7.5, heated at 95°C for 5 min and then allowed to cool to room temperature. Primer extension reactions (10 μl) contained 25 mM HEPES pH 8.0, 5 mM 2-mercaptoethanol, 50 μg/ml BSA, 5 mM $MgCl_2$, 25 μM each dNTP, 2 nM labeled primer-template substrate, and 0 or 150 mM NaCl, as

indicated. Pol γ holoenzyme components were preassembled on ice with 25 nM PolG and 50 nM PolG2 variant. Reactions were initiated by addition (2 μl) of pre-mixed holoenzyme components to final concentrations of 5 nM PolG and 10 nM PolG2, followed by incubation at 37°C for 20 min. Reactions were placed on ice, quenched by addition (10 μl) of formamide solution (45% deionized formamide, 10 mM EDTA pH 8.0, 2.5 mg/ml bromophenol blue, 2.5 mg/ml xylene cyanol), and boiled for 3 min. Samples (17 μl) of each stopped reaction were resolved by electrophoresis on 1% alkaline agarose gels (0.5 × 20 × 25 cm) containing 30 mM NaOH and 1mM EDTA at 30 V for 16–18 h. Gels were transferred to Whatman paper, dried, and imaged using a phosphor storage screen and a Typhoon FLA 9500 scanner (Cytiva). Reactions utilizing M462C PolG2 were assembled as above and contained either 0 or 2 mM 2-mercaptoethanol, as indicated in the figure legends.

Steady-state kinetics

DNA polymerase activity of PolG was determined for preassembled holoenzymes with poly(rA)•oligo(dT)$_{12–18}$ and dTTP as substrates, essentially as described (14). The primer-template was produced by annealing oligo(dT)$_{12–18}$ and poly(rA) at an equimolar A:T ratio by heating to 95°C in 10 mM Tris–HCl (pH 7.5), followed by slow cooling. Reactions (50 μl) containing 25 mM HEPES–KOH (pH 7.5), 2.5 mM 2-mercaptoethanol, 0.5 mM $MnCl_2$, 200 μg/ml heat-treated BSA, 16 μCi/ml [α-^{32}P]dTTP, 50 μg/ml poly(rA)•oligo(dT)$_{12–18}$ (5280 nM primer termini), 220 mM NaCl, varying concentrations of dTTP (0, 0.5, 1, 1.5, 2, 2.5, 3, 5, 10, 15, 20, 25 μM) and a fixed concentration of Pol γ holoenzyme (1 nM PolG and 2 nM PolG2) were incubated at 37°C for 0, 3, 6, 8 and 10 min. Reactions were stopped by the addition of 1 mg/ml BSA in 0.1 M NaPPi (0.2 ml) and cold 10% TCA (1 ml). Samples were then filtered through Whatman GF/C filters, washed with 1 N HCl, rinsed with 100% ethanol and dried before TCA-insoluble radioactivity was determined by liquid scintillation counting.

The binding affinity between PolG and PolG2 variants was determined in identical reactions, except the dTTP concentration was fixed at 25 μM and reactions contained varied ratios of PolG and PolG2. Separate mixtures of Pol γ holoenzyme components were preassembled on ice, and reactions were initiated by addition (5 μl) of pre-mixed holoenzyme components to final concentrations of 2.5 nM PolG and 0–25 nM PolG2 variant. Reactions were incubated for 9 min and processed as before. Apparent $K_{d(PolG)}$ values were derived by nonlinear regression of holoenzyme activity isotherms, as described for EMSAs.

RESULTS

Atomic force microscopy imaging of human PolG2 and DNA

Visualization of purified human PolG2 in the absence of DNA by atomic force microscopy (AFM) reveals a uniform field of spatially resolved particles (Figure 1A). The AFM volumes of particles (n = 275) show a Gaussian distribution centered at 111 ± 48 nm^3 (Gaussian peak ± S.D.) (Figure 1B). Because the AFM volumes of globular proteins increase linearly with molecular weight (36), this single-molecule volume determination shows that dimeric PolG2 is the prominent species in solution, in agreement with previous ensemble biochemical analyses (21). We next used AFM to characterize the nature of PolG2–DNA complexes with a model DNA replication fork substrate consisting of circular duplex DNA, a dsDNA/ssDNA fork junction, and an extended dsDNA tail (28,37) (Figure 1C). Analysis of >500 PolG2–DNA complexes (Figure 1D) shows that 57% of the bound PolG2 is distributed along either the circular or linear (tail) contour of the DNA substrate. Whereas 35% and 8% of the bound PolG2 is specifically at the fork junction or the end of the dsDNA tail, respectively (Figure 1E). The disproportionate presence of PolG2 bound to artificial replication fork junctions in our AFM images is consistent with previous results of electrophoretic mobility shift assays (EMSA) showing preferential binding of PolG2 to synthetic D-loop structures (23).

More interestingly, the average AFM volume of PolG2–DNA complexes varies considerably among different binding regions (Figure 1F). The average volume of complexes along the circular contour of the dsDNA substrate (n = 180) is 147 ± 98 nm^3, which is marginally larger than free PolG2 dimers, whereas the volume of complexes at the fork junction (n = 131) is 226 ± 166 nm^3. PolG2 structures bridging two separate DNA substrate molecules are clearly visible in some AFM images (Figure 1G). The AFM volumes of these complexes (n = 156) split into two populations of 271 ± 148 nm^3 and 479 ± 121 nm^3 (Figure 1F), with the higher value matching the expected AFM volume of PolG2 hexamers (441 nm^3). Collectively, the AFM data indicate that PolG2 is a dimer in solution, binds dsDNA as a dimer, and can form higher order PolG2 oligomers upon binding fork junctions or bridging two DNA molecules.

X-ray crystal structures of PolG2–DNA complexes

To define the molecular basis of PolG2–DNA interactions, we crystallized and determined two murine PolG2–DNA complexes: (i) hexameric PolG2 engaging two 18-bp duplexes (Figure 2A–C, and Supplementary Figures S1 and S3A) and, (ii) dimeric PolG2 bound to an 18-bp palindromic DNA (Supplementary Figures S2 and S3B). Overall, the hexamer is organized as a trimer of PolG2 dimers. A central dimer (Chains A/B) organizes the hexamer assembly by scaffolding two added flanking dimers (Chains C/D and E/F, Figure 2A–C) that are related to the central PolG2 pair by pseudo two-fold symmetry (Figure 2D). Together, six PolG2 chains engage two 18-bp palindromic DNA duplexes (Figure 2A and C). In the crystalline lattice, the PolG2 hexamer is positioned at the center of a 'criss-crossed' DNA superstructure (Supplementary Figure S4). In a second crystal form, dimeric PolG2 binds to a single copy of the 18 bp duplex (Supplementary Figure S2). These two PolG2 DNA binding architectures are consistent with AFM observations that place dimeric PolG2 engaging linear DNA duplexes and multimeric PolG2 assemblies at the nexus of forked and crossed DNA assemblies (Figure 1).

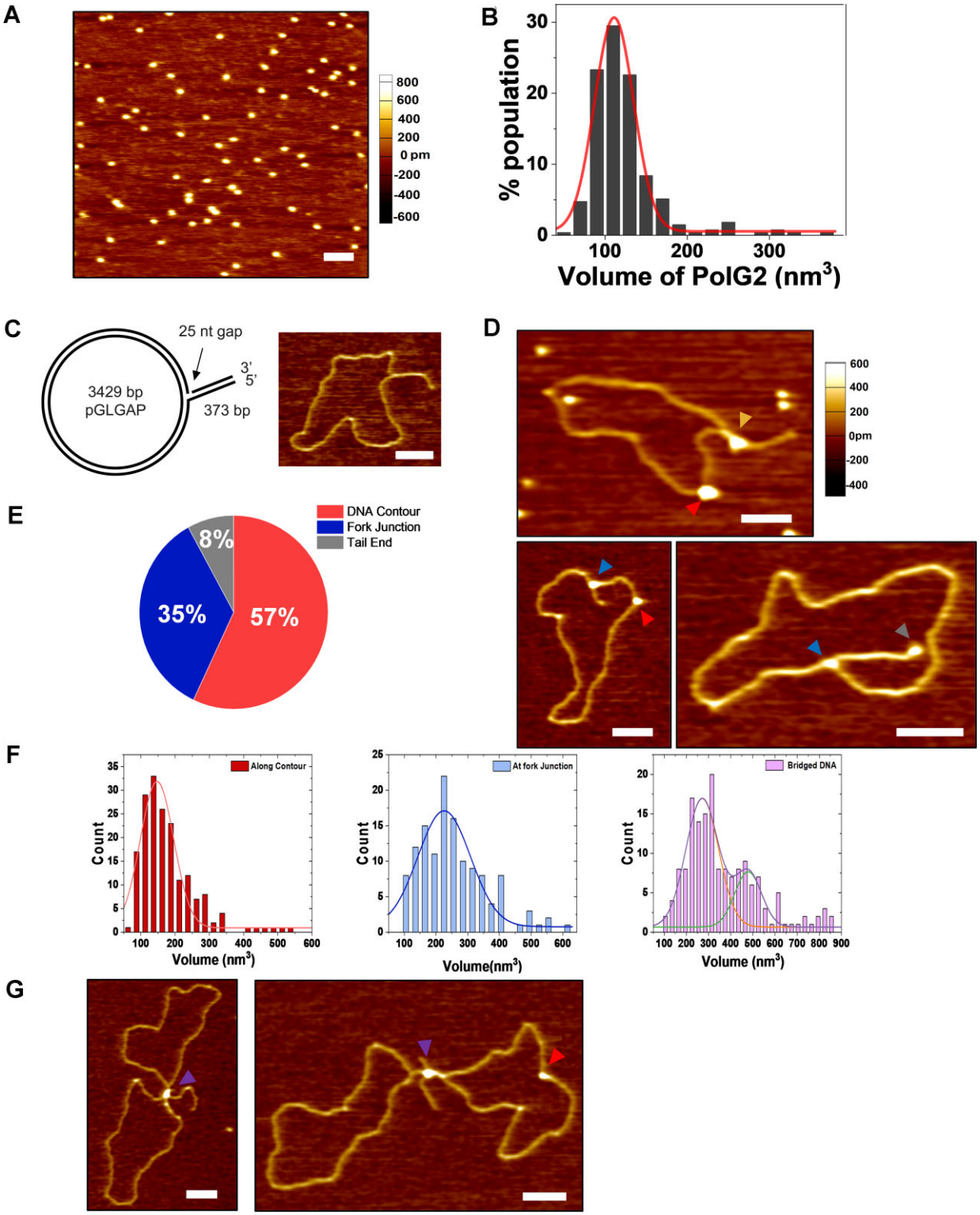

Figure 1. Visualization of human PolG2 alone and binding to model DNA replication fork structures using AFM imaging. (**A**) Representative AFM topographic image of PolG2 protein. (**B**) AFM volume distribution ($n = 275$) of PolG2 fit with a Gaussian function ($R^2 = 0.98$). (**C**) Schematic (left panel) and representative AFM image (right panel) of the model DNA replication fork substrate containing a duplex circle (3429 bp) with a dsDNA tail (373 bp) and a 25 nt ssDNA gap at the junction of the circle and the tail. (**D**) Representative AFM images of PolG2 protein binding different structures on the model DNA substrate. Structures are identified with color-coded arrows as in panel (E). (**E**) Fraction of PolG2–DNA complexes present at specific structures of the forked DNA substrate. (**F**) AFM volumes of PolG2–DNA complexes present at different structures of the model replication fork substrate. Complexes bridging two substrate molecules split into two volume populations. The lines represent Gaussian fits to the data with peaks centered at 147 (± 98) nm^3 for along the contour, 226 (± 166) nm^3 for at the fork junction, 271 (± 148) nm^3 and 479 (± 121) nm^3 for bridged DNA. $R^2 > 0.84$. (**G**) Representative AFM images of PolG2 binding separate substrate molecules to create intermolecular DNA bridges (purple arrows). All X–Y scale bars are 100 nm.

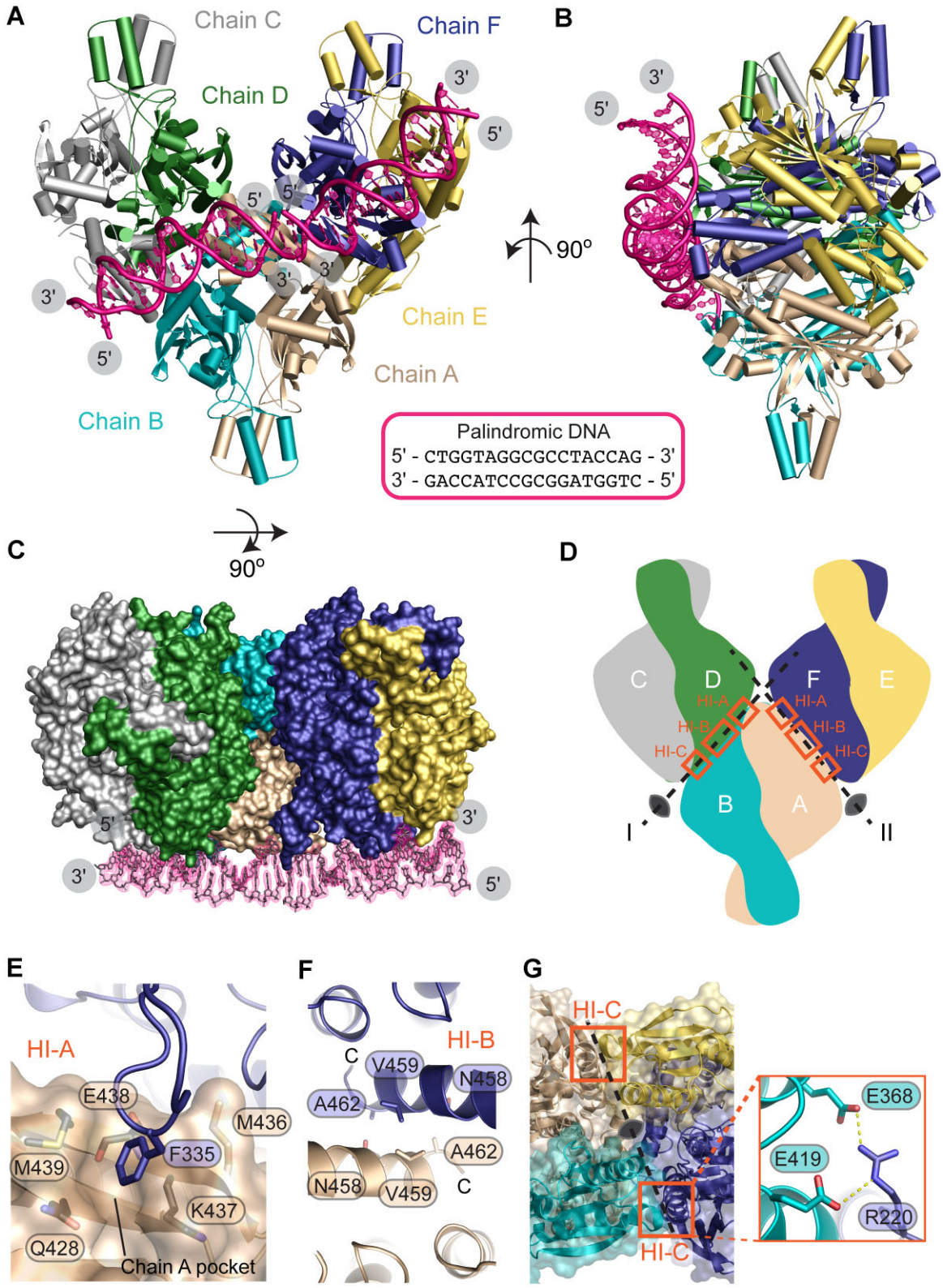

Figure 2. Overview of the DNA-bound hexameric PolG2 crystal structure. (**A**) The asymmetric unit of the hexamer crystal is made up of six chains of mouse PolG2 and two palindromic dsDNAs shown in hot pink. (**B**) An orthogonal view of (A). (**C**) An alternate orthogonal view of (A) with the hexamer in surface representation and the 2Fo-Fc electron density map of the DNA contoured at 1.5σ. (**D**) Schematic of the central PolG2 dimer (Chains A/B) forming pseudo 2-fold symmetric interactions with the left and right flanking PolG2 dimers within a trimer of dimers (hexamer). The axes of pseudo symmetry are labeled I and II. Between two PolG2 dimers, there are three unique interfaces of interaction, labeled HI-A, B and C (Hexamer Interfaces A–C). (**E**) A zoomed in view of HI-A where the sidechain of F335 of Chain F is buried into a surface pocket of Chain A. (**F**) A zoomed in view of HI-B where the C-terminal helices of Chain F and Chain A symmetrically cross one another. (**G**) A view of the pseudo 2-fold symmetry at HI-C. HI-C is characterized by charge complementarity between Chain F R220 and Chain B E368 and E419 sidechains.

The hexameric PolG2 trimer of dimers

Within the PolG2 hexamer, each pseudo 2-fold axis (gray axes I and II, Figure 2D), is comprised of three hexamer stabilizing interfaces (HI-A, B and C) that combine to bury ∼2100 Å^2 of solvent-accessible surface area per axis. In HI-A, F335 extends to bind a flanking PolG2 dimer hydrophobic surface pocket lined by Q428, K437 and M439 and the backbone of E438 (Figure 2E). HI-B assembles via hydrophobic anti-parallel C-terminal α17 helix-helix interactions mediated by residues N458 and V459 (Native to PolG2), and A462 from the expression tag (Figure 2F). Notably, a *POLG2* disease-linked frameshift (L475DfsX2) deletes HI-B (Supplementary Figure S5). While HI-A and HI-B occur once per axis, two copies of HI-C reinforce the hexameric assembly and contribute two pairs of interdigitating salt-bridges from R220 to E368 and E419 (Figure 2G).

To probe the functional significance of PolG2 multimerization, we employed a structure-guided Cys–Cys disulfide crosslinking strategy to engineer and manipulate PolG2 oligomer status (Figure 3). Based on modeling, we predicted that the closely juxtaposed M436 side chains in the context of the PolG2 hexamer would form a reactive interchain disulfide crosslink when mutated to cysteine (Figure 3B–C). The murine and human PolG2 amino acid sequence is 79% identical and 89% similar in homology. As the hydrophobic hexameric interface is conserved (Figure 3E and Supplementary Figure S5), we generated a human M462C PolG2 mutant for biochemical analyses. Size exclusion chromatography coupled to multi-angle light scattering (SEC-MALS) reveals WT PolG2 is dimeric as anticipated, either in the presence (MW = 107 ± 0.8% kDa) or absence (MW = 108 ± 0.6% kDa) of 1 mM TCEP reducing agent (Figure 3D). The M462C PolG2 mutant is also predominantly dimeric in solution either in the presence (MW = 115 ± 1.4% kDa) or absence (MW = 125 ± 9.8% kDa) of TCEP (Figure 3D). However, without reducing reagent, M462C PolG2 assembles into additional stable oligomeric species of sizes 240 ± 6.7% kDa and 380 ± 4.7% kDa, that are most consistent with tetramers and higher-order oligomers ($N = 6$–8) (Figure 3D). The M462C PolG2 tetrameric species is also observed in 1 mM TCEP, suggesting the engineered disulfide is relatively stable.

To test the impact of DNA binding on PolG2 oligomerization, we titrated WT and M462C PolG2 with a 47bp dsDNA substrate and monitored PolG2-PolG2 disulfide bond formation by SDS-PAGE. In this context, while WT PolG2 resolves as a monomer on non-reducing SDS-PAGE, M462C PolG2 exists as a mixture of monomers and disulfide dimers, establishing that formation of the covalent dimer is diagnostic for assembly of protein-protein contacts via the hexamerization interface (Figure 3F, lanes 1 and 9). This hexameric interface disulfide crosslinked dimer is preserved under non-reducing conditions, but dimerization is reversed by incubation with >1% 2-mercaptoethanol (Supplementary Figure S6A). Titration of 47 bp dsDNA with M462C PolG2, but not WT PolG2, increases the intensity of the disulfide-crosslinked band approximately 2-fold, consistent with dsDNA binding stabilizing PolG2 oligomerization via the hexamerization interface (Figure 3F, G). In control reactions, NaCl titration partially attenuates dsDNA-stimulated disulfide dimer formation, likely due to disruption of PolG2 nucleic acid binding (Supplementary Figure S6B, lanes 8–13). Overall, results from AFM, X-ray structures and disulfide crosslinking analysis suggest that the PolG2 dimer can assemble into higher order oligomers including hexamers, and this interaction is promoted by dsDNA binding.

PolG2 binds DNA via four DNA binding regions

Within the three PolG2 domains (Domains 1–3, Figure 4A), four PolG2 DNA-binding regions (DBRs) map to the C-terminus of Domain 1 (DBR1) and throughout Domain 3 (DBRs 2–4, Figure 4A–E). By contrast, the PolG2 dimerization helical bundle (Domain 2) does not directly participate in either DNA binding or hexamerization (Figures 2A and 4B). DBR1 from one PolG2 protomer and DBRs 2–4 of the second PolG2 in a PolG2 dimer bind to the same 18 bp dsDNA (Figure 4D). Within the hexamer, Dimer E/F binds the first dsDNA molecule while Dimers A/B and C/D engage the second dsDNA molecule (Supplementary Figure S1A).

A survey of the DNA binding interactions shows an intricate and extensive DNA binding surface. Furthermore, a high degree of sequence conservation of DNA binding residues is observed for all four DBRs (Figure 4C, Supplementary Figure S5). The DBR1 loops (Figure 4E, yellow Chain E) engages the minor groove with R302 making hydrogen bonds to the oxygens of bases dC^{15}, dT^5 and the deoxyribose sugar of dA^6. R299 and K303 hydrogen bond to the backbone phosphate oxygens to reinforce the DBR1-DNA interface (Supplementary Figure S1B and C). DBR3 and DBR4 together engage the major groove of the DNA (Figure 4DE, Supplementary Figure S1E and F). DBR3 R370 hydrogen bonds to the phosphate oxygens of dG^8 and K363 to the base of dG^{10}. T366 packs against the sugar of dG^8 whilst its backbone nitrogen hydrogen bonds to the phosphate oxygen of dC^9 at N-terminal end of the α13 helix dipole (Figure 4E, Supplementary Figure S1B and S1E). In DBR4 (Chain F), H396 hydrogen bonds to the bases of dG^8 and dG^{10} and T394 hydrogen bonds with the backbone phosphate oxygen of dG^7. S398 caps helix α15 whose dipole moment aligns to the phosphate oxygens of dG^8 (Figure 4E, Supplementary Figure S1B and S1F).

Interestingly, DBR2 binds DNA in the hexamer via an extended loop conformation at the junction of the two DNA duplexes in the crystal. Key DNA-binding residues of DBR2 are R337, which both base stacks with the 5′ terminal residue of one 18-mer DNA and hydrogen bonds to the base of the 3′ terminal dG^{18} of the second duplex, while K338 hydrogen bonds to the phosphate oxygen of dC^{16} (Figure 4E, F, Supplementary Figure S1B and D). By comparison, in the PolG2–dimer DNA complex structure, DBR2 is contracted and in a helical conformation that is not engaged with DNA (Figure 4G). These conformational differences are coincident with bending of the DNA substrate in the hexameric form compared to the PolG2 dimer bound structure (Figure 4F). Additional residues in the DBR2 loop facilitate DNA binding and hexamer protein-protein contacts. R343 (R369 in humans) stabilizes the

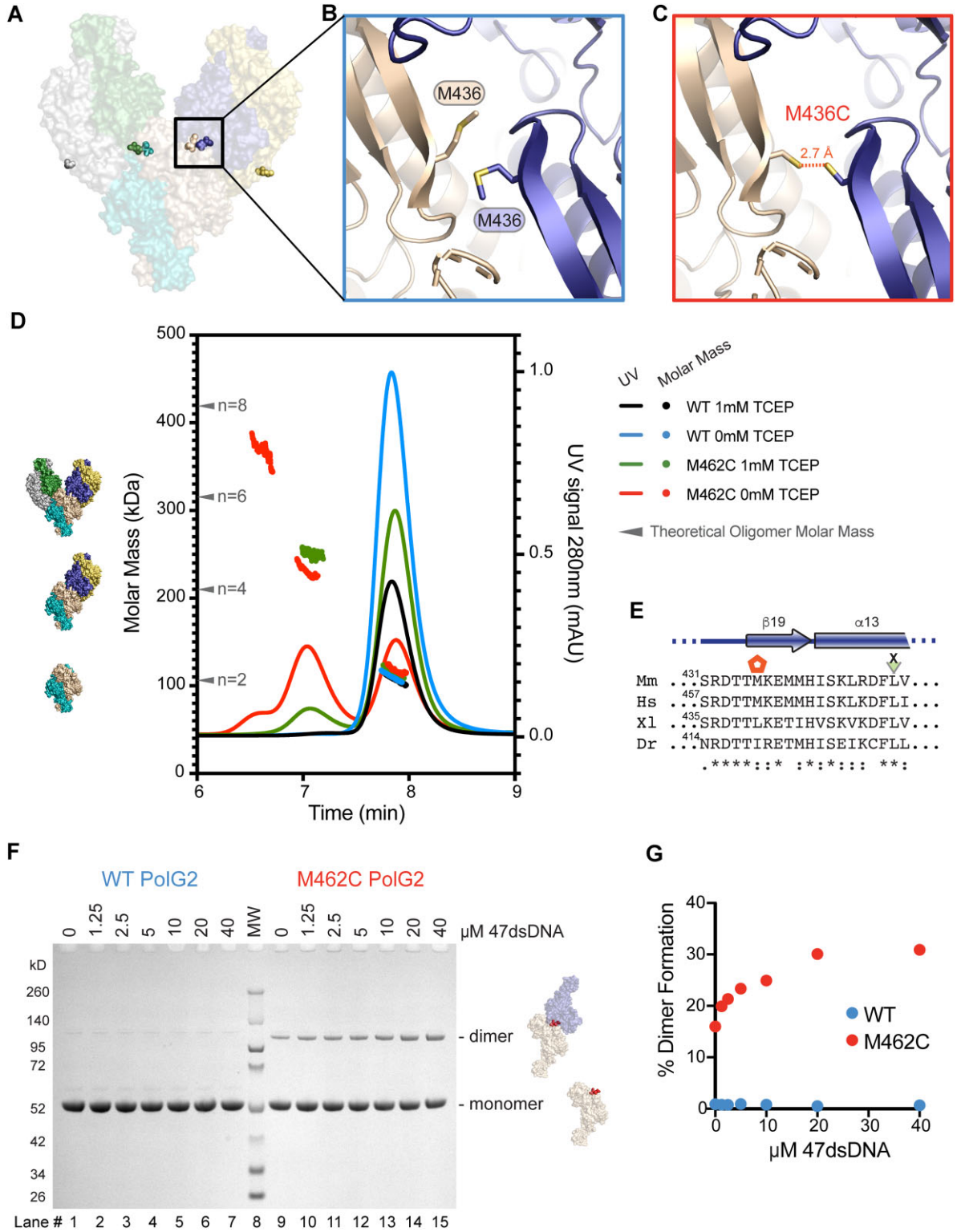

Figure 3. An engineered disulfide provides evidence of PolG2 higher-order oligomerization in solution that is stimulated by dsDNA. (**A**) Mouse PolG2 hexamer structure with the M436 residues from all six chains indicated. (**B**) A zoomed in view of the close proximity of M436 residues adjacent to HI-A establishing candidacy for an engineered disulfide within the PolG2 hexamer assembly. (**C**) Model of the mutation of M436 to cysteine within the mouse hexamer PolG2 structure by PyMOL. (**D**) DNA-free SECMALS results for human WT versus M462C PolG2 in the presence of either 0 or 1 mM TCEP. (**E**) Sequence alignment and residue conservation for the C-terminal region of PolG2. The PolG2 secondary structure is diagramed above. The methionine residue mutated to a cysteine in both the mouse and human PolG2 constructs is denoted with an orange hexagon. A human PolG2 clinical mutation resulting in a C-terminal truncation is denoted with a green wedge. Mm is *Mus musculus*, Hs is *Homo sapiens*, Xl is *Xenopus laevis*, and Dr is *Danio rerio*. (**F**) Formation of the engineered disulfide at the hexamer interface in human PolG2 is stimulated by dsDNA as shown in a denaturing SDS-PAGE gel free of reducing reagent. (**G**) The percent disulfide-dimer formed was calculated from the gel in panel F using Image Lab and graphed in Prism.

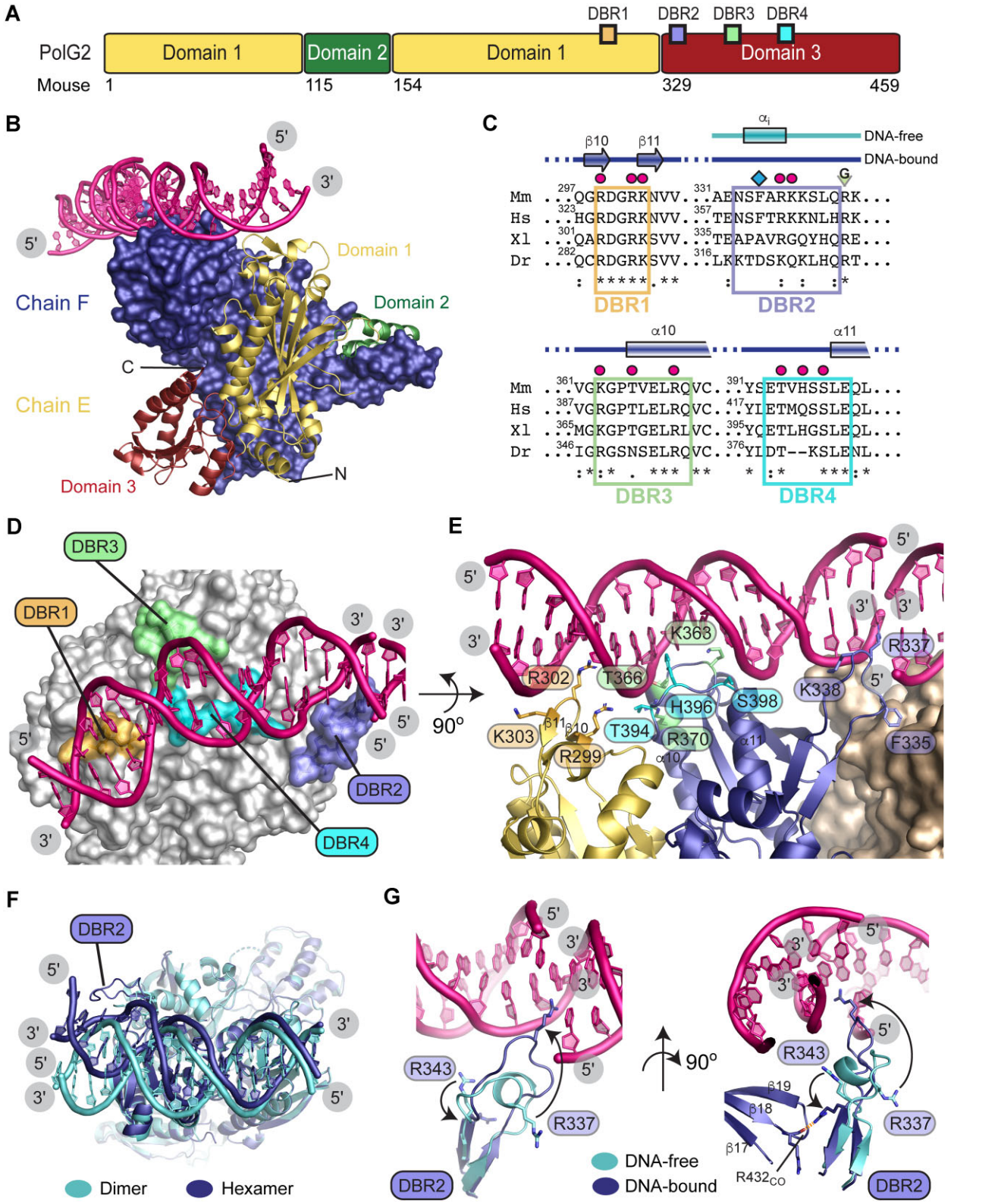

Figure 4. PolG2 DNA-binding interactions. (**A**) Domain diagram of PolG2. (**B**) Domain boundaries of PolG2 shown on the structure in ribbon diagram for Chain E. (**C**) Sequence alignment and residue conservation for DBRs 1–4. The PolG2 secondary structure of DNA-bound Chain F is diagramed above. DNA binding residues are denoted with a pink circle. Inter-domain stabilizing residue F335 is labeled with a blue diamond. Human PolG2 clinical mutations are denoted with a green wedge. Mm is *Mus musculus*, Hs is *Homo sapiens*, Xl is *Xenopus laevis*, and Dr is *Danio rerio*. (**D**) Locations of the DBRs are noted on the E/F PolG2 dimer in gray surface representation. (**E**) DNA-binding residues are labeled within the DBRs of Chain E (yellow ribbon) and Chain F (deep blue ribbon). Surface representation of Chain A is shown in wheat. (**F**) The dsDNA bends when in complex with the DBR2 of PolG2 within a hexamer P32 crystal form (deep blue) relative to when bound to the simple PolG2 dimer (cyan) as seen in the P422 crystal form. (**G**) DBR2 conformation ranges drastically between a DNA-free tightly packed helical structure (cyan) to a DNA-bound fully-extended loop (deep blue).

Table 1. DBR alanine substitutions in human PolG2 and corresponding mouse residue numbers

DBR alanine substitutions made in Human PolG2	Human residue numbers	Mouse residue numbers
DBR1-Ala: VSKLHGADGAANVVPCV	R325A, R328A, K329A	R299A, R302A, K303A
DBR2-Ala: ENSFTAAANLHRK	R363A, K364A, K365A	R337A, K338A, K339A
DBR3-Ala: VALDVGAGPALELAQVCQGL	R389A, T392A, R396A	K363A, T366A, R370A
DBR4-Ala: WPGYLEAMASALEQLYSK	T420A, Q422A, S424A	T394A, H396A, S398A

Ala protein variants for each DBR were created by mutagenesis of human *POLG2* expression vectors, as described in Online Methods.

extended DBR2 loop conformation by hydrogen bonding to the backbone carbonyl of R432, allowing R337 to extend and contact DNA (Figure 4G), while F335 participates in the HI-A interaction interface (Figure 4E). That the human R369G PolG2 disease variant maps adjacent to DBR2 implies this substitution destabilizes this DNA-bound extended DBR2 loop (Figure 4C and G, Supplementary Figure S5). This notion is supported by prior biochemical data indicating decreased dsDNA binding affinity for R369G PolG2 homodimers ($K_{d(DNA)}$ is 86 ± 50 nM) relative to WT PolG2 ($K_{d(DNA)}$ is 49 ± 25 nM) (13). In sum, structural data point to DBR2 mediating DNA binding and hexamer assembly via a dynamic, regulated DNA binding mechanism impacted in a PolG2 disease variant.

Functional assessment of DBR-substituted PolG2 proteins

DNA binding affinity. To test functional roles of PolG2 DNA binding surfaces, DNA binding residues in each DBR (Figure 4 and Supplementary Figure S1) were substituted with alanine (Table 1), and DNA binding was evaluated by quantitative EMSA (Figure 5A). WT PolG2 exhibited an equilibrium disassociation constant ($K_{d(dsDNA)}$) of 44.0 ± 7.3 nM. Mutation of DBR1 or DBR2 ablated DNA binding at all concentrations tested, corroborating previous reports (21,22). By contrast, the PolG2$^{DBR3\text{-}Ala}$ and PolG2$^{DBR4\text{-}Ala}$ mutants had apparent $K_{d(dsDNA)}$ values of 2760 ± 430 nM and 102 ± 19 nM, respectively, representing 63-fold ($P < 0.001$, $n = 4$) and 2.3-fold ($P < 0.04$, $n = 3$) weaker affinity for dsDNA than WT PolG2. Thus, all four DBRs identified in the hexamer crystal structure differentially contribute to dsDNA binding *in vitro*.

Stimulation of DNA synthesis by PolG. The PolG2 accessory subunit increases the affinity of DNA binding in the Pol γ holoenzyme by over 100-fold, increases processivity of DNA synthesis several 100-fold, allowing for the salt tolerance of the Pol γ holoenzyme (8,9). Thus, we tested whether the highly varied DNA binding affinities of the PolG2 DBR-Ala mutants influenced DNA synthesis by PolG. The ability of PolG paired with each PolG2 DBR-Ala mutant to extend an end-labeled primer annealed to M13 DNA *in vitro* was monitored by alkaline agarose gel electrophoresis (Figure 5B) and urea–PAGE gel (Supplementary Figure S7). As expected from previous reports (8,27), primer extension activity of isolated PolG (lane 2) was completely inhibited by 150 mM NaCl, which promotes disassociation of PolG from DNA. However, addition of PolG2^{WT} permitted efficient extension of primers to kilobase lengths (compare lanes 2 and 3) and nearly complete depletion of available primers. Both the quantity and length of primer extension products were severely reduced in reactions utilizing PolG2$^{DBR1\text{-}Ala}$ and PolG2$^{DBR2\text{-}Ala}$ (lanes 4 and 5). Extended primers in reactions with PolG2$^{DBR2\text{-}Ala}$ were scarcely more abundant than products of isolated PolG. Reactions with PolG2$^{DBR3\text{-}Ala}$ and PolG2$^{DBR4\text{-}Ala}$ also generated long products, although primer utilization was less efficient than with PolG2^{WT} (compare lanes 6 & 7 to lane 3). Overall, there is a general correlation between PolG2 DNA binding affinity and the ability to stimulate DNA synthesis by PolG.

Our results only partially align with a previous report showing that DNA binding deficient PolG2$^{DBR1\text{-}Ala}$ and PolG2$^{DBR2\text{-}Ala}$ mutants can stimulate DNA synthesis by PolG on poly(dA)•oligo(dT) *in vitro* (22). This apparent contradiction may be because primer extension of end-labeled primers in our alkaline agarose gel assay requires processive DNA synthesis, rather than distributive DNA synthesis on homopolymer substrates. To test this, we compared stimulation of PolG by PolG2^{WT}, PolG2$^{DBR1\text{-}Ala}$ and PolG2$^{DBR2\text{-}Ala}$ dimers in reactions that compel distributive DNA synthesis and maximize catalytic cycling of Pol γ holoenzyme. Conditions included a high concentration of short, fully duplex poly(rA)•oligo(dT)$_{12–18}$ homopolymeric substrate and suppression of isolated PolG activity by high salt, which constrain activity to PolG2-dependent DNA synthesis by holoenzyme complexes (8,13). Rates of DNA synthesis for PolG-PolG2 complexes were determined at varied dTTP concentrations (Figure 5C), and steady state kinetic parameters were calculated according to the Michaelis-Menten model, as described previously (14). Holoenzymes assembled with PolG2^{WT} ($K_{M(dTTP)}$ = 1.29 ± 0.12 μM, k_{cat} = 25.5 ± 1.39 min^{-1}) or PolG2$^{DBR1\text{-}Ala}$ ($K_{M(dTTP)}$ = 1.64 ± 0.23 μM, k_{cat} = 24.3 ± 1.23 min^{-1}) had similar kinetic parameters, suggesting intrinsic DNA binding by PolG2 is not essential to stimulate distributive DNA synthesis. By comparison, PolG-PolG2$^{DBR2\text{-}Ala}$ complexes had a similar $K_{M(dTTP)}$ = 1.69 ± 0.09 μM, but a 2-fold diminished k_{cat} = 12.5 ± 0.63 min^{-1} ($P = 0.001$, $n = 3$). Because the distal PolG2 monomer enhances holoenzyme formation and supports an increased polymerization rate of WT Pol γ (19), this 2-fold slower steady-state turnover for Pol γ assembled with DBR2-Ala PolG2 may reflect impaired DNA contacts for the holoenzyme or an altered conformation of the distal DBR2-Ala PolG2 monomer. We conclude that PolG2 DNA binding is important for processive, but not distributive, DNA synthesis.

Physical interaction with PolG. Comparing WT Pol γ structures in a DNA-free state or bound in a ternary complex with dCTP and DNA implied that DNA-binding induces a conformational change that significantly extends interaction of PolG with the distal PolG2 subunit (20). To assess whether DBR1-Ala- or DBR2-Ala-substitutions

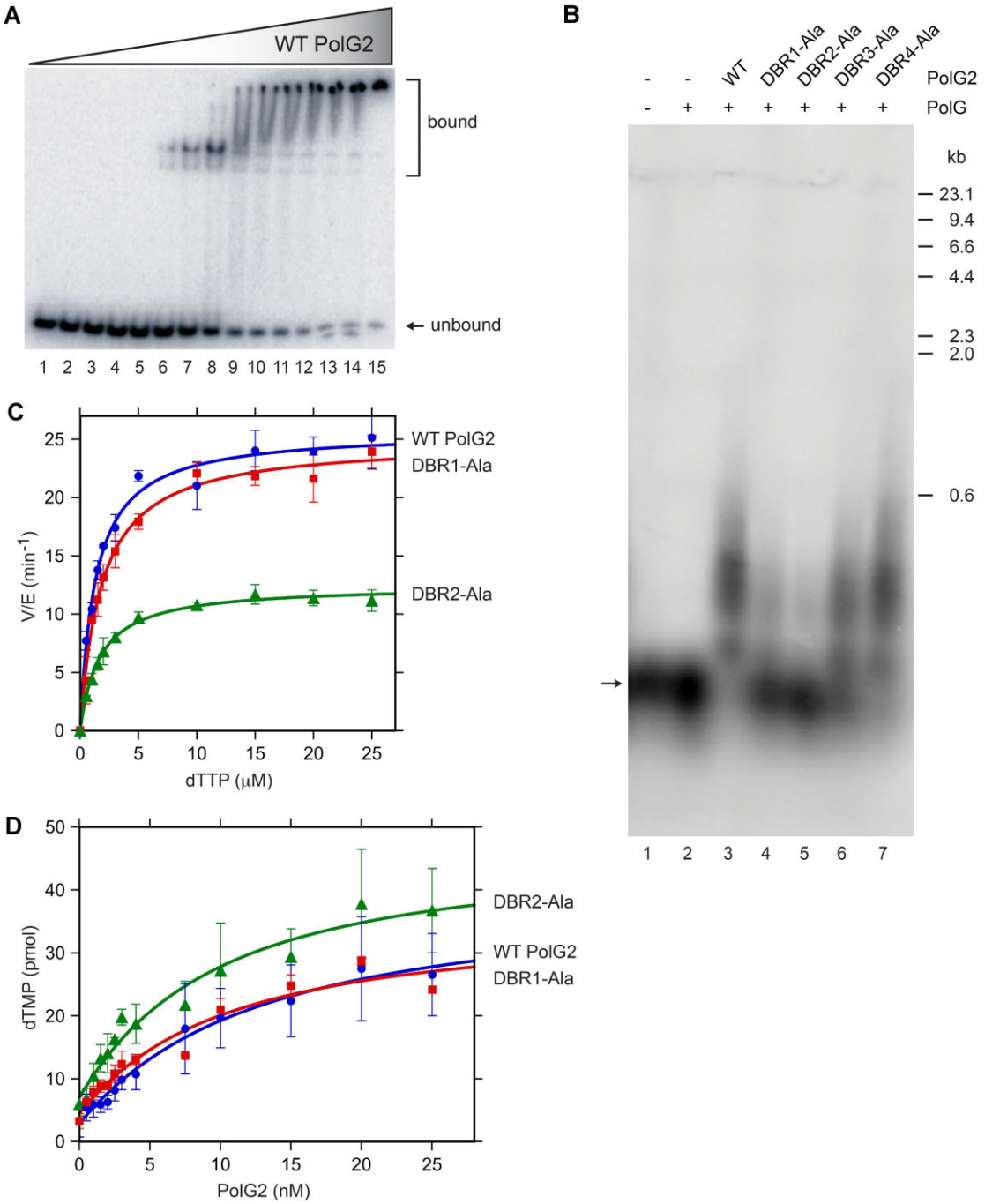

Figure 5. Functional assessment of DBR-substituted PolG2 proteins. (**A**) The DNA binding affinity of WT and DNA binding mutant PolG2 proteins was determined by Electrophoretic Mobility Shift Assay. Lanes 1–15 in the representative gel image contained 0, 6.25, 12.5, 18.8, 25, 62.5, 125, 250, 625, 1250, 1875, 2500, 3750, 5000 and 14900 nM WT PolG2. Equilibrium binding constants were calculated from the fraction of double-stranded 47mer oligonucleotide bound at each protein concentration, as described in Online Methods. (**B**) The ability of PolG2 proteins to stimulate DNA synthesis by PolG *in vitro* was assessed in primer extension assays followed by alkaline agarose gel electrophoresis. Reactions contained 150 mM NaCl and no enzymes (lane 1) or PolG (lanes 2–7) with WT PolG2 (lane 3), DRB1-Ala PolG2 (lane 4), DRB2-Ala PolG2 (lane 5), DRB3-Ala PolG2 (lane 6) or DRB4-Ala PolG2 (lane 7), as described in the Online Methods. The migration position of end-labeled 35mer primer (arrow) and estimated positions of HindIII-digested bacteriophage λ DNA size markers are indicated. (**C**) The effects of DBR1-Ala and DBR2-Ala PolG2 on the steady state kinetics of dTMP incorporation by PolG were assessed in DNA synthesis reactions with fully duplex poly(rA)•oligo(dT)$_{12–18}$ as substrate, as described in Online Methods. Apparent k_{cat} values derived from triplicate determinations (average ± SEM) for PolG paired with WT PolG2 (*circles*), DBR1-Ala PolG2 (*squares*), or DBR2-Ala PolG2 (*triangles*) dimers were 25.5 ± 1.39, 24.3 ± 1.23 and 12.5 ± 0.63 min^{-1}, respectively. (**D**) The inter-subunit binding affinities of PolG for WT, DBR1-Ala and DBR2-Ala PolG2 were determined in DNA synthesis reactions containing 2.5 nM PolG and the indicated concentrations of PolG2 monomers, as described in Online Methods. Binding isotherms were generated by plotting holoenzyme activity at each concentration of PolG2. Equilibrium disassociation constants were calculated by nonlinear regression from at least three independent determinations. Apparent $K_{d(PolG)}$ values (average ± SEM) for WT PolG2 (*circles*), DBR1-Ala PolG2 (*squares*), and DBR2-Ala PolG2 (*triangles*) were 8.65 ± 2.57, 13.0 ± 3.04 and 7.30 ± 3.14 nM, respectively.

altered PolG-PolG2 protein-protein interactions, we measured inter-subunit binding affinities with a modified activity assay. As with the steady state kinetics measurements, holoenzyme reaction conditions were chosen so that association of PolG and PolG2 was required for robust activity. DNA synthesis reactions utilized a fixed concentration of WT PolG (2.5 nM) with increasing quantities of PolG2, and inter-subunit equilibrium disassociation constants were estimated from holoenzyme activity isotherms (Figure 5D). The apparent $K_{d(PolG)}$ values for assembly of active holoenzyme from PolG and PolG2^{WT}, PolG2$^{DBR1\text{-}Ala}$ or PolG2$^{DBR2\text{-}Ala}$ were comparable at 8.65 ± 2.57, 13.0 ± 3.04 and 7.30 ± 3.14 nM, respectively. This uniformity of inter-subunit affinities is consistent with efficient catalytic cycles for each holoenzyme during distributive DNA synthesis (Figure 5C), and it also shows that alanine substitution in DBR1 and DBR2 impairs processive DNA synthesis (Figure 5B) without diminishing Pol γ inter-subunit affinities.

Functional assessment of M462-substituted PolG2 proteins. We next exploited the ability to modulate the PolG2^{M462C} oligomeric state using sulfhydryl reducing agents (Figure 3) to test the effects of PolG2 oligomerization on DNA binding affinity. Samples of PolG2^{M462C} that had been purified in the presence or absence of sulfhydryl reducing agents were evaluated by EMSA, and equilibrium disassociation constants were calculated as before from their respective binding isotherms (Figure 6A). Reduced PolG2^{M462C} ($K_{d(dsDNA)}$ = 40.4 ± 12 nM) had an equilibrium binding constant comparable to PolG2^{WT} ($K_{d(dsDNA)}$ = 44.0 ± 7.3 nM, $P \approx 0.79$, $n = 3$). However, the apparent $K_{d(dsDNA)}$ for non-reduced PolG2^{M462C} was 5.7-fold weaker ($K_{d(dsDNA)}$ = 251 ± 26 nM, $P < 0.0005$, $n = 3$) than PolG2^{WT}, suggesting that stabilization of higher order PolG2 oligomers decreases overall DNA binding affinity. The degree to which DNA-binding facilitates formation of higher order PolG2 assemblies was estimated with the Hill equation. Whereas reduced PolG2^{M462C} had a Hill coefficient of 1.28 ± 0.13, non-reduced PolG2^{M462C} exhibited a visibly sigmoidal binding curve with a Hill coefficient of 3.57 ± 0.65, consistent with a concentration-dependent, stable oligomerization of PolG2^{M462C} in the absence of reducing agents.

To probe roles for PolG2 oligomerization in DNA synthesis, we tested PolG–PolG2^{M462C} complexes using our primer extension assay. Both primer utilization and the lengths of end-labeled primer extension products were monitored by alkaline agarose gel electrophoresis (Figure 6B). In reactions containing supplemental 2-mercaptoethanol, isolated PolG was inhibited by 150 mM NaCl, as expected (compare lanes 2 and 7). Holoenzymes assembled with PolG2^{WT} or reduced PolG2^{M462C} both generated kilobase length DNA synthesis products, and primer utilization was robust at 150 mM NaCl (compare lanes 3 and 4 to lanes 8 and 9). Despite the presence of supplemental 2-mercaptoethanol in the reaction, PolG2^{M462C} purified in the absence of reducing agent could not stimulate primer extension by PolG at either 0 or 150 mM NaCl (lanes 5 and 10). The lengths of reaction products at 0 mM NaCl resembled those of PolG alone (lanes 2 and 5), implying failure to form an active holoenzyme with non-

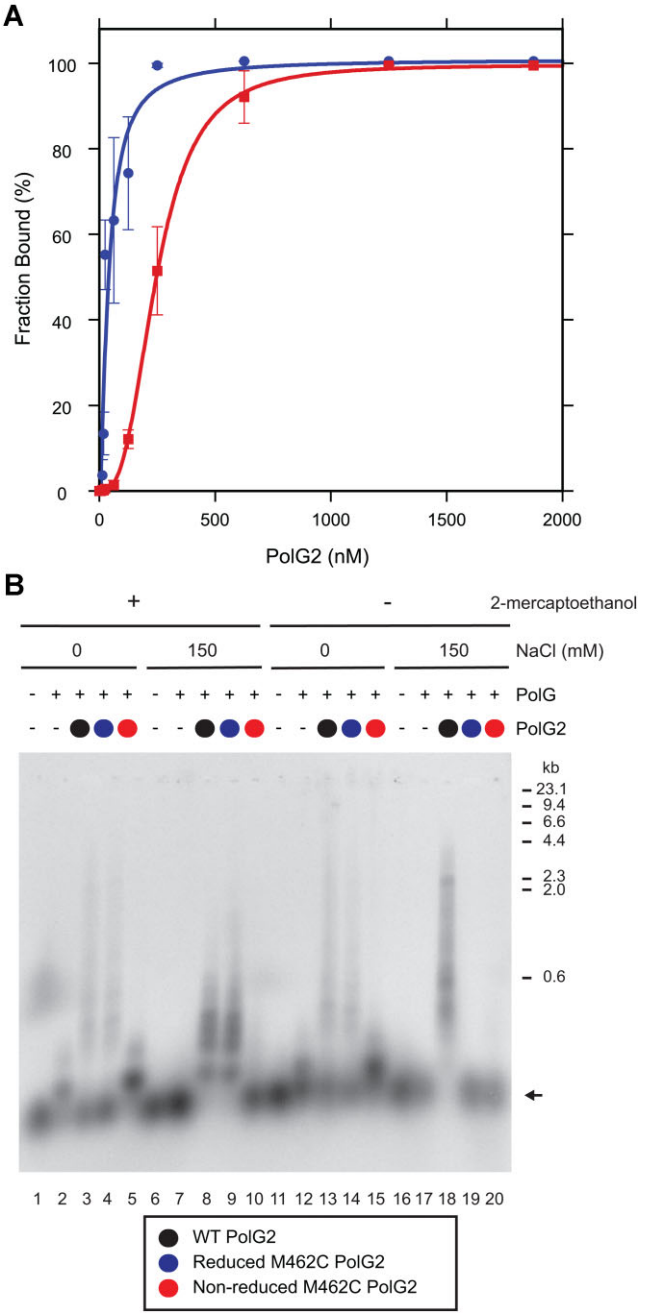

Figure 6. Functional assessment of M462C-substituted PolG2 proteins. (**A**) The DNA binding affinity of M462C PolG2 oligomers was assessed by EMSA, as described in Online Methods. Binding isotherms for reduced M462C PolG2 (purified with 2-mercaptoethanol, *blue circles*) and non-reduced M462C PolG2 (purified without 2-mercaptoethanol, *red squares*) were constructed by plotting the fraction of 47mer dsDNA substrate bound at the indicated protein concentrations. Error bars are the SEM of triplicate determinations. (**B**) Stimulation of DNA synthesis by PolG was assessed in primer extension assays followed by alkaline agarose gel electrophoresis, as described in Online Methods. Reactions included either 0 mM or 2 mM 2-mercaptoethanol, and also 0 mM or 150 mM NaCl, as indicated. Reactions were assembled with the following combinations of proteins: no enzyme control (lanes 1, 6, 11, 16), PolG (lanes 2–5, 7–10, 12–15, 17–20), WT PolG2 (lanes 3, 8, 13, 18), reduced M462C PolG2 (lanes 4, 9, 14, 19), or non-reduced M462C PolG2 (lanes 5, 10, 15, 20). The migration position of end-labeled 35mer primer (arrow) and estimated positions of HindIII-digested bacteriophage λ DNA size markers are indicated.

reduced PolG2^{M462C} (lanes 5 and 10). Reactions lacking supplemental 2-mercaptoethanol were performed in parallel, and primer extension products for reactions with 0 mM NaCl (lanes 11–15) matched those made in the presence of added 2-mercaptoethanol (lanes 1–5). Although primer extension reactions for holoenzyme assembled with PolG2^{WT} were maximally efficient at 150 mM NaCl (lanes 8 and 18), the absence of supplemental 2-mercaptoethanol coincided with a complete loss of stimulatory function for reduced PolG2^{M462C} (compare lanes 9 and 19). The dependence of PolG-reduced-PolG2^{M462C} holoenzyme activity on supplemental 2-mecaptoethanol suggests loss of function may be driven by rapid reoxidation of sulfhydryl groups within the time span of the reaction. Such conversion to the inactive, non-reduced form of PolG2^{M462C} (lanes 5, 10, 15, 20) would also facilitate oligomerization of PolG2 by restoring interchain disulfide crosslinks at the hexamer interface.

DISCUSSION

Overall, our AFM, X-ray structural, and biochemical data indicate that PolG2–DNA binding has both PolG-dependent and -independent functions. PolG2 exists as an obligate dimer in solution that is in dynamic DNA-stimulated equilibrium with higher order tetrameric and hexameric assemblies. The delineation of the PolG2 DNA binding mechanism has unveiled highly conserved DNA interaction interfaces that are critical to PolG2 functions in mitochondrial DNA maintenance. Structural and mutational data implicate the PolG2 DNA interaction surface in supporting its canonical role as an accessory factor for PolG DNA synthesis. Our observations extend published results that defined how PolG2 scaffolds a carboxy-terminal L-helix element of PolG that facilitates DNA binding of the PolG-PolG2 holoenzyme (Figure 7). We posit that the PolG2 DNA binding surface characterized here further enhances processivity of the holoenzyme, as mutations in the PolG2 DNA binding surfaces impair PolG-PolG2 processive DNA synthesis, but not PolG interactions (Figure 5). In this scenario, additional DNA contacts to PolG2 might be mediated by a DNA looping mechanism that facilitates processive DNA synthesis by the holoenzyme (Figure 7A).

Analysis of clinical variants outlines the complexity of PolG-dependent roles for PolG2. Compared to WT PolG2, the homodimeric R369G PolG2 disease variant exhibits reduced binding affinity both to dsDNA and to the PolG catalytic subunit, which contribute to a concomitant reduction in the efficiency of stimulating primer extension by PolG *in vitro* (13,38). These observations are consistent with our structural predictions that R369G substitution influences DNA-binding and PolG2 hexamerization by destabilizing the extended loop in DBR2. Similarly, the L475DfsX2 PolG2 frameshift disease variant truncates PolG2 and removes HI-B and three PolG2 residues that interact with PolG (Supplementary Figure S5), which aligns with the failure of L475DfsX2 PolG2 to bind dsDNA or to bind and stimulate the PolG catalytic subunit *in vitro* (13). However, PolG2 heterodimers formed by coupling WT PolG2 monomers with either R369G or L475DfsX2 disease variant monomers are able to stimulate PolG processivity *in vitro* as efficiently as WT PolG2 homodimers (35), which suggests stimulation requires specific contacts between PolG and the WT PolG2 monomer. In contrast, G451E PolG2 homodimers fail to form a holoenzyme with PolG (12), and WT/G451E PolG2 heterodimers exert a dominant negative biochemical effect on DNA synthesis *in vitro* (35). Because PolG is predicted to interact with conserved G451 residues in both the proximal and distal PolG2 protomers, G451E substitution in just one PolG2 monomer has the potential to disrupt holoenzyme function, which correlates with the dominant mode of inheritance of the human G451E *POLG2* disease allele. The predicted structural significance for a selection of clinically identified mitochondrial disease variants in human PolG2 are listed in Supplementary Table S2.

Notably, the architecture of the PolG–PolG2 complex is incompatible with engagement of a PolG2 hexamer. Structural overlays of the PolG2 hexamer structure with the PolG–PolG2–DNA complex (PDB: 4ZTU) (20) illustrate a significant clash would occur between the L-helix of the PolG AID subdomain and PolG2 hexamerization interfaces HI-B and HI-C (Figure 7B). These results imply that the hexameric PolG2 DNA-binding states observed in X-ray and AFM may play additional roles in mitochondrial DNA maintenance other than support of ongoing mtDNA synthesis (e.g. acting as an architectural DNA binding protein or regulating specific protein traffic at the D-loop). As an essential component of the mtDNA replisome, PolG2 is a precise spatial marker for mitochondrial nucleoids actively engaged in mtDNA replication *in vivo* (35,39). Earlier work by Holt and coworkers showed that knockdown of *POLG2* expression by siRNA in cultured human cells reduces mtDNA copy number but increases nucleoid numbers, whereas *POLG2* over-expression reduces nucleoid numbers while increasing their size. Intriguingly, both depletion and overexpression of PolG2 caused a loss of 7S DNA (23). Interestingly, a recent study using a disease model of PolG in mice found that free PolG is degraded by the mitochondrial LonP protease (40). Quantitative Western blot analysis in this study demonstrated that PolG2 exists in superstoichiometric levels relative to PolG in both human and mouse tissues. They found that the PolG2 dimer exist in 4–15-fold molar excess to PolG (40). These measurements further suggest complex roles for PolG2 in the propagation of mitochondrial nucleoids, maintenance of mtDNA D-loops, and regulation of mtDNA synthesis.

We postulate that PolG2 fulfills these roles through specific interactions at forked DNA structures on both ends of the mitochondrial D-loop. For example, a PolG2 dimer bound to forked DNA may form a protein-protein complex upon encountering PolG or another PolG2 dimer. Addition of PolG permits formation of a replication-competent heterotrimeric Pol γ holoenzyme. In this scenario, PolG2 acts as a fork recognition factor to recruit PolG to the D-loop for extension of RNA primers or 7S DNA, as previously suggested (8,41,42). Alternatively, accretion of another PolG2 dimer by oligomerization excludes PolG. In this scenario, PolG2 participates in maintenance of the D-loop by stabilizing the forked DNA structure and perhaps protecting the 5′ and 3′ ends of 7S DNA from degradation by MGME1 or PolG exonuclease (43–46). Similarly,

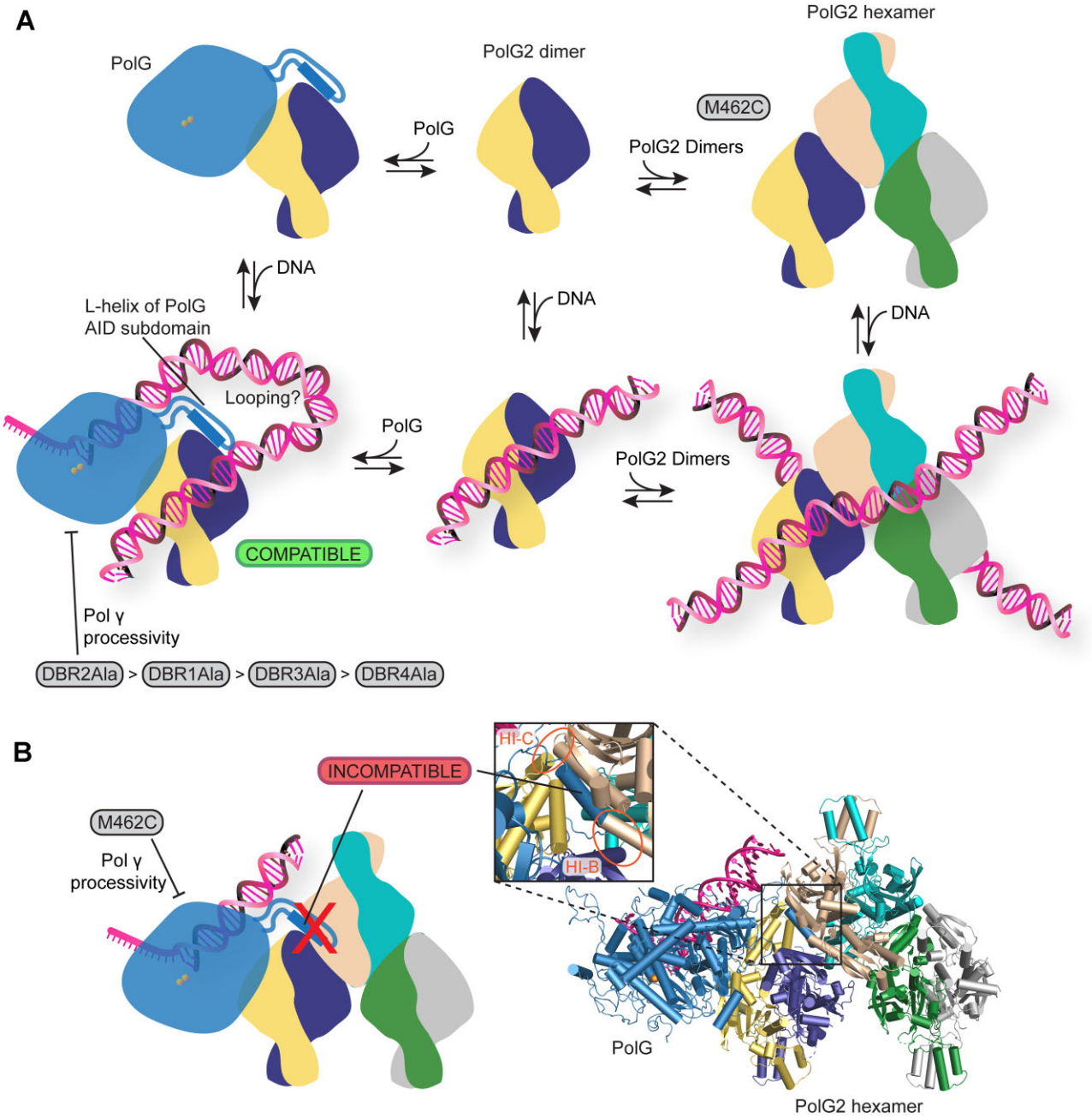

Figure 7. Model for PolG dependent and independent roles of PolG2. (**A**) PolG2 DNA-binding is compatible with PolG-dependent activity as indicated by the DBRAla mutants with deficient DNA binding having reduced PolG stimulation. The M462C PolG2 mutant stabilizes the hexamer. (**B**) The architecture of the PolG-PolG2 complex is incompatible with engagement of a PolG2 hexamer. Structural overlays of the PolG2 hexamer structure with the PolG–PolG2–DNA complex (PDB 4ZTU) illustrate a significant clash would occur between the L-helix of the PolG AID subdomain and PolG2 HI-B and HI-C. The non-reduced M462C PolG2 mutant is deficient in supporting PolG activity compared to wild type PolG2.

if PolG2 bound at the 5′-end of the D-loop can extract the PolG2 dimer from an approaching replicative Pol γ holoenzyme, then the remaining PolG subunit becomes incapable of strand displacement DNA synthesis (47). In any event, our structural and biochemical data imply that formation of holoenzyme heterotrimers and PolG2 hexamers are mutually exclusive and competitive, which suggests a vital role for PolG2 as a biological switch between mtDNA replication and maintenance functions.

DATA AVAILABILITY

Structures and associated experimental data for the dimeric (8F69) and hexameric (8F6B) murine PolG2–DNA complexes were deposited in the RCSB Protein Data Bank.

SUPPLEMENTARY DATA

Supplementary Data are available at NAR Online.

ACKNOWLEDGEMENTS

We thank Drs Amanda A. Riccio and Scott A. Lujan for critical reading of this manuscript. X-ray diffraction data were collected at Southeast Regional Collaborative Access Team (SER-CAT) 22-ID beamline at the Advanced Photon Source, Argonne National Laboratory. We thank Lars Pedersen of the NIEHS Structural Biology Core, and the Advanced Photon Source (APS) Southeast Regional Collaborative Access Team (SER-CAT) staff for assistance with crystallographic data collection.

FUNDING

Intramural Research Program of the NIEHS, National Institutes of Health [Z01ES065078 to W.C.C., Z01ES102765 to R.S.W.]; Extramural Research Program of the National Institutes of Health [R01GM107559, R21ES027641, R01GM123246 to H.W.]; North Carolina State University Center for Human Health and the Environment Pilot Project [P30ES025128 to P.K., H.W.]; use of the Advanced Photon Source was supported by the U.S. Department of Energy, Office of Science, Office of Basic Energy Sciences [W-31-109-Eng-38]. Funding for open access charge: National Institute of Environmental Health Science.
Conflict of interest statement. None declared.

REFERENCES

1. Anderson,S., Bankier,A.T., Barrell,B.G., de Bruijn,M.H., Coulson,A.R., Drouin,J., Eperon,I.C., Nierlich,D.P., Roe,B.A., Sanger,F. *et al.* (1981) Sequence and organization of the human mitochondrial genome. *Nature*, **290**, 457–465.
2. Fish,J., Raule,N. and Attardi,G. (2004) Discovery of a major D-loop replication origin reveals two modes of human mtDNA synthesis. *Science*, **306**, 2098–2101.
3. Doda,J.N., Wright,C.T. and Clayton,D.A. (1981) Elongation of displacement-loop strands in Human and mouse mitochondrial-DNA is arrested near specific template sequences. *Proc. Natl. Acad. Sci. U.S.A.*, **78**, 6116–6120.
4. Kasamatsu,H., Robberson,D.L. and Vinograd,J. (1971) A novel closed-circular mitochondrial DNA with properties of a replicating intermediate. *Proc. Natl. Acad. Sci. U.S.A.*, **68**, 2252–2257.
5. Nicholls,T.J. and Minczuk,M. (2014) In D-loop: 40 years of mitochondrial 7S DNA. *Exp. Gerontol.*, **56**, 175–181.
6. Korhonen,J.A., Pham,X.H., Pellegrini,M. and Falkenberg,M. (2004) Reconstitution of a minimal mtDNA replisome in vitro. *EMBO J.*, **23**, 2423–2429.
7. Graziewicz,M.A., Longley,M.J. and Copeland,W.C. (2006) DNA polymerase gamma in mitochondrial DNA replication and repair. *Chem. Rev.*, **106**, 383–405.
8. Lim,S.E., Longley,M.J. and Copeland,W.C. (1999) The mitochondrial p55 accessory subunit of human DNA polymerase gamma enhances DNA binding, promotes processive DNA synthesis, and confers N-ethylmaleimide resistance. *J. Biol. Chem.*, **274**, 38197–38203.
9. Johnson,A.A., Tsai,Y., Graves,S.W. and Johnson,K.A. (2000) Human mitochondrial DNA polymerase holoenzyme: reconstitution and characterization. *Biochemistry*, **39**, 1702–1708.
10. Young,M.J. and Copeland,W.C. (2016) Human mitochondrial DNA replication machinery and disease. *Curr. Opin. Genet. Dev.*, **38**, 52–62.
11. Suomalainen,A. and Battersby,B.J. (2018) Mitochondrial diseases: the contribution of organelle stress responses to pathology. *Nat. Rev. Mol. Cell Biol.*, **19**, 77–92.
12. Longley,M.J., Clark,S., Yu Wai Man,C., Hudson,G., Durham,S.E., Taylor,R.W., Nightingale,S., Turnbull,D.M., Copeland,W.C. and Chinnery,P.F. (2006) Mutant POLG2 disrupts DNA polymerase gamma subunits and causes progressive external ophthalmoplegia. *Am. J. Hum. Genet.*, **78**, 1026–1034.
13. Young,M.J., Longley,M.J., Li,F.Y., Kasiviswanathan,R., Wong,L.J. and Copeland,W.C. (2011) Biochemical analysis of human POLG2 variants associated with mitochondrial disease. *Hum. Mol. Genet.*, **20**, 3052–3066.
14. Hoff,K.E., DeBalsi,K.L., Sanchez-Quintero,M.J., Longley,M.J., Hirano,M., Naini,A.B. and Copeland,W.C. (2018) Characterization of the human homozygous R182W POLG2 mutation in mitochondrial DNA depletion syndrome. *PLoS One*, **13**, e0203198.
15. Landrum,M.J., Lee,J.M., Benson,M., Brown,G.R., Chao,C., Chitipiralla,S., Gu,B., Hart,J., Hoffman,D., Jang,W. *et al.* (2018) ClinVar: improving access to variant interpretations and supporting evidence. *Nucleic Acids Res.*, **46**, D1062–D1067.
16. Karczewski,K.J., Francioli,L.C., Tiao,G., Cummings,B.B., Alfoldi,J., Wang,Q., Collins,R.L., Laricchia,K.M., Ganna,A., Birnbaum,D.P. *et al.* (2020) The mutational constraint spectrum quantified from variation in 141,456 humans. *Nature*, **581**, 434–443.
17. Humble,M.M., Young,M.J., Foley,J.F., Pandiri,A.R., Travlos,G.S. and Copeland,W.C. (2013) Polg2 is essential for mammalian embryogenesis and is required for mtDNA maintenance. *Hum. Mol. Genet.*, **22**, 1017–1025.
18. Lee,Y.S., Kennedy,W.D. and Yin,Y.W. (2009) Structural insight into processive human mitochondrial DNA synthesis and disease-related polymerase mutations. *Cell*, **139**, 312–324.
19. Lee,Y.S., Lee,S., Demeler,B., Molineux,I.J., Johnson,K.A. and Yin,Y.W. (2010) Each monomer of the dimeric accessory protein for human mitochondrial DNA polymerase has a distinct role in conferring processivity. *J. Biol. Chem.*, **285**, 1490–1499.
20. Szymanski,M.R., Kuznetsov,V.B., Shumate,C., Meng,Q., Lee,Y.S., Patel,G., Patel,S. and Yin,Y.W. (2015) Structural basis for processivity and antiviral drug toxicity in human mitochondrial DNA replicase. *EMBO J.*, **34**, 1959–1970.
21. Carrodeguas,J.A., Theis,K., Bogenhagen,D.F. and Kisker,C. (2001) Crystal structure and deletion analysis show that the accessory subunit of mammalian DNA polymerase gamma, pol gamma B, functions as a homodimer. *Mol. Cell*, **7**, 43–54.
22. Carrodeguas,J.A., Pinz,K.G. and Bogenhagen,D.F. (2002) DNA binding properties of human pol gammaB. *J. Biol. Chem.*, **277**, 50008–50014.
23. Di Re,M., Sembongi,H., He,J., Reyes,A., Yasukawa,T., Martinsson,P., Bailey,L.J., Goffart,S., Boyd-Kirkup,J.D., Wong,T.S. *et al.* (2009) The accessory subunit of mitochondrial DNA polymerase gamma determines the DNA content of mitochondrial nucleoids in human cultured cells. *Nucleic Acids Res.*, **37**, 5701–5713.
24. Fan,L., Kim,S., Farr,C.L., Schaefer,K.T., Randolph,K.M., Tainer,J.A. and Kaguni,L.S. (2006) A novel processive mechanism for DNA synthesis revealed by structure, modeling and mutagenesis of the accessory subunit of human mitochondrial DNA polymerase. *J. Mol. Biol.*, **358**, 1229–1243.
25. DeBalsi,K.L., Longley,M.J., Hoff,K.E. and Copeland,W.C. (2017) Synergistic effects of the in cis T251I and P587L mitochondrial DNA polymerase gamma disease mutations. *J. Biol. Chem.*, **292**, 4198–4209.
26. Kasiviswanathan,R., Longley,M.J., Young,M.J. and Copeland,W.C. (2010) Purification and functional characterization of human mitochondrial DNA polymerase gamma harboring disease mutations. *Methods*, **51**, 379–384.
27. Longley,M.J., Ropp,P.A., Lim,S.E. and Copeland,W.C. (1998) Characterization of the native and recombinant catalytic subunit of human DNA polymerase gamma: identification of residues critical for exonuclease activity and dideoxynucleotide sensitivity. *Biochemistry*, **37**, 10529–10539.
28. Subramanian,D. and Griffith,J.D. (2005) p53 Monitors replication fork regression by binding to “chickenfoot” intermediates. *J. Biol. Chem.*, **280**, 42568–42572.
29. Kaur,P., Longley,M.J., Pan,H., Wang,W., Countryman,P., Wang,H. and Copeland,W.C. (2020) Single-molecule level structural dynamics of DNA unwinding by human mitochondrial twinkle helicase. *J. Biol. Chem.*, **295**, 5564–5576.
30. Kaur,P., Pan,H., Longley,M.J., Copeland,W.C. and Wang,H. (2021) Using atomic force microscopy to study the real time dynamics of DNA unwinding by mitochondrial twinkle helicase. *Bio Protoc*, **11**, e4139.
31. Otwinowski,Z. and Minor,W. (1997) Processing of X-ray diffraction data collected in oscillation mode. *Methods Enzymol.*, **276**, 307–326.

32. Adams,P.D., Afonine,P.V., Bunkoczi,G., Chen,V.B., Davis,I.W., Echols,N., Headd,J.J., Hung,L.W., Kapral,G.J., Grosse-Kunstleve,R.W. *et al.* (2010) PHENIX: a comprehensive Python-based system for macromolecular structure solution. *Acta. Crystallogr. D Biol. Crystallogr.*, **66**, 213–221.
33. Emsley,P. and Cowtan,K. (2004) Coot: model-building tools for molecular graphics. *Acta. Crystallogr. D Biol. Crystallogr.*, **60**, 2126–2132.
34. Heyduk,T. and Lee,J.C. (1990) Application of fluorescence energy transfer and polarization to monitor Escherichia coli cAMP receptor protein and lac promoter interaction. *Proc. Natl. Acad. Sci. U.S.A.*, **87**, 1744–1748.
35. Young,M.J., Humble,M.M., DeBalsi,K.L., Sun,K.Y. and Copeland,W.C. (2015) POLG2 disease variants: analyses reveal a dominant negative heterodimer, altered mitochondrial localization and impaired respiratory capacity. *Hum. Mol. Genet.*, **24**, 5184–5197.
36. Kaur,P., Wu,D., Lin,J., Countryman,P., Bradford,K.C., Erie,D.A., Riehn,R., Opresko,P.L. and Wang,H. (2016) Enhanced electrostatic force microscopy reveals higher-order DNA looping mediated by the telomeric protein TRF2. *Sci. Rep.*, **6**, 20513.
37. Countryman,P., Fan,Y., Gorthi,A., Pan,H., Strickland,J., Kaur,P., Wang,X., Lin,J., Lei,X., White,C. *et al.* (2018) Cohesin SA2 is a sequence-independent DNA-binding protein that recognizes DNA replication and repair intermediates. *J. Biol. Chem.*, **293**, 1054–1069.
38. Craig,K., Young,M.J., Blakely,E.L., Longley,M.J., Turnbull,D.M., Copeland,W.C. and Taylor,R.W. (2012) A p.R369G POLG2 mutation associated with adPEO and multiple mtDNA deletions causes decreased affinity between polymerase gamma subunits. *Mitochondrion*, **12**, 313–319.
39. Lewis,S.C., Uchiyama,L.F. and Nunnari,J. (2016) ER-mitochondria contacts couple mtDNA synthesis with mitochondrial division in human cells. *Science*, **353**, aaf5549.
40. Silva-Pinheiro,P., Pardo-Hernandez,C., Reyes,A., Tilokani,L., Mishra,A., Cerutti,R., Li,S., Rozsivalova,D.H., Valenzuela,S., Dogan,S.A. *et al.* (2021) DNA polymerase gamma mutations that impair holoenzyme stability cause catalytic subunit depletion. *Nucleic Acids Res.*, **49**, 5230–5248.
41. Fan,L., Sanschagrin,P.C., Kaguni,L.S. and Kuhn,L.A. (1999) The accessory subunit of mtDNA polymerase shares structural homology with aminoacyl-tRNA synthetases: implications for a dual role as a primer recognition factor and processivity clamp. *Proc. Natl. Acad. Sci. U.S.A.*, **96**, 9527–9532.
42. Carrodeguas,J.A. and Bogenhagen,D.F. (2000) Protein sequences conserved in prokaryotic aminoacyl-tRNA synthetases are important for the activity of the processivity factor of human mitochondrial DNA polymerase. *Nucleic Acids Res.*, **28**, 1237–1244.
43. Kornblum,C., Nicholls,T.J., Haack,T.B., Scholer,S., Peeva,V., Danhauser,K., Hallmann,K., Zsurka,G., Rorbach,J., Iuso,A. *et al.* (2013) Loss-of-function mutations in MGME1 impair mtDNA replication and cause multisystemic mitochondrial disease. *Nat. Genet.*, **45**, 214–219.
44. Matic,S., Jiang,M., Nicholls,T.J., Uhler,J.P., Dirksen-Schwanenland,C., Polosa,P.L., Simard,M.L., Li,X., Atanassov,I., Rackham,O. *et al.* (2018) Mice lacking the mitochondrial exonuclease MGME1 accumulate mtDNA deletions without developing progeria. *Nat. Commun.*, **9**, 1202.
45. Uhler,J.P., Thorn,C., Nicholls,T.J., Matic,S., Milenkovic,D., Gustafsson,C.M. and Falkenberg,M. (2016) MGME1 processes flaps into ligatable nicks in concert with DNA polymerase gamma during mtDNA replication. *Nucleic Acids Res.*, **44**, 5861–5871.
46. Nissanka,N., Bacman,S.R., Plastini,M.J. and Moraes,C.T. (2018) The mitochondrial DNA polymerase gamma degrades linear DNA fragments precluding the formation of deletions. *Nat. Commun.*, **9**, 2491.
47. Sullivan,E.D., Longley,M.J. and Copeland,W.C. (2020) Polymerase gamma efficiently replicates through many natural template barriers but stalls at the HSP1 quadruplex. *J. Biol. Chem.*, **295**, 17802–17815.